



# In Situ Investigation of Structural Evolution in $Zr_{46}Cu_{46}Al_8$ and $Zr_{56}Cu_{36}Al_8$ Bulk Metallic Glasses During Isothermal Annealing

XUELIAN WU<sup>1,2</sup>, XIYANG LI<sup>2,3</sup>, ZHENDUO WU<sup>4</sup>, XUN-LI WANG<sup>2</sup>,  
XIAOYA WEI<sup>5</sup>, JIE ZHOU<sup>6</sup>, ZHAOPING LU<sup>6</sup>, ELLIOT PAUL GILBERT<sup>7</sup>,  
ZHENGMING SUN<sup>1,8</sup>, JIANXIANG DING<sup>1,8,10</sup>, DONGMING LIU<sup>1,11</sup>,  
CHENCHEN YUAN<sup>8,12</sup> and SI LAN<sup>2,9,13</sup>

1.—Advanced Ceramics Research Center, School of Materials Science and Engineering, Anhui University of Technology, No. 59 Hudong Road, Ma'anshan 243032, Anhui, China. 2.—Department of Physics, City University of Hong Kong, Hong Kong 999077, China. 3.—Department of Physics & Astronomy and Stewart Blusson Quantum Matter Institute, University of British Columbia, Vancouver, BC V6T 1Z4, Canada. 4.—Center for Neutron Scattering and Applied Physics, City University of Hong Kong Dongguan Research Institute, Dongguan 523000, China. 5.—Institute of Advanced Science Facilities, Shenzhen 518107, Guangdong, China. 6.—State Key Laboratory for Advanced Metals and Materials, University of Science and Technology Beijing, Beijing 100083, China. 7.—Australian Centre for Neutron Scattering, Australian Nuclear Science and Technology Organisation, Lucas Heights, NSW 2234, Australia. 8.—Jiangsu Key Laboratory of Advanced Metallic Materials, School of Materials Science and Engineering, Southeast University, Nanjing 211189, Jiangsu, China. 9.—School of Materials Science and Engineering, Herbert Gleiter Institute of Nanoscience, Nanjing University of Science and Technology, Nanjing 210094, Jiangsu, China. 10.—e-mail: jxding@ahut.edu.cn. 11.—e-mail: ldm1975@ahut.edu.cn. 12.—e-mail: yuance@seu.edu.cn. 13.—e-mail: lans@njjust.edu.cn

The crystallization kinetics of  $Zr_{46}Cu_{46}Al_8$  and  $Zr_{56}Cu_{36}Al_8$  bulk metallic glasses (BMGs) during isothermal annealing in the supercooled liquid region has been studied using in situ simultaneous differential scanning calorimetry (DSC) and small-angle neutron scattering (SANS) technique.  $Zr_{46}Cu_{46}Al_8$ , known for its good glass forming ability (GFA), exhibits a complex crystallization pathway. Initially, a transition region emerges, eventually evolving into the thermodynamically stable crystalline phase of  $Cu_{10}Zr_7$ , facilitated by continuous chemical redistribution at the late stage of annealing. In contrast,  $Zr_{56}Cu_{36}Al_8$ , a poor glass former, crystallizes directly into the thermodynamically stable crystalline phase of  $CuZr_2$  in a single step, with no observed chemical redistribution. Overall, the results suggest that continuous chemical redistribution following structural ordering may contribute to stabilizing the amorphous state and improving the thermal stability of BMGs. This study highlights the critical role of chemical redistribution in the crystallization of BMGs and introduces a new perspective for assessing their GFAs.

## INTRODUCTION

Upon isothermal annealing in the supercooled liquid region, a bulk metallic glass (BMG) typically crystallizes, resulting in a microstructure characterized by a high number density of nanoscale

precipitates embedded in the remaining amorphous matrix. This process has garnered significant interest for its implications for the understanding of glass formation and the development of materials with superior properties.

Zr-Cu-Al BMG, as a cost-effective alloy with excellent mechanical properties and glass forming ability (GFA), has attractive characteristics for potential application in the field of structural materials. Its slow crystallization kinetics, simple

(Received May 30, 2024; accepted July 22, 2024)

chemical composition, and wide supercooled liquid phase region render it an ideal model system for research.<sup>1-6</sup> Extensive investigations have been conducted to explore the crystallization process of Zr-Cu-Al BMGs within the supercooled liquid region. For example, Lan et al.<sup>7</sup> examined the isothermal crystallization behaviors of  $Zr_{56}Cu_{36}Al_8$  and  $Zr_{46}Cu_{46}Al_8$  BMGs, discovering that the former underwent continuous nucleation and growth, whereas the latter exhibited site-saturated nucleation followed by slow growth. Later, phase separation prior to crystallization was identified in  $Zr_{46}Cu_{46}Al_8$  BMG during isothermal annealing in the supercooled liquid region.<sup>8</sup> Further comprehensive studies of crystallization kinetics in various Zr-Cu-Al BMGs with different GFAs showed a transition from classic to avalanche modes of nucleation upon isothermal annealing. The classic mode is characterized by a continuous nucleation and growth of  $Zr_2Cu$ -type crystals, while the avalanche mode features an abrupt formation of massive  $Cu_{10}Zr_7$ -type precipitates with a less ordered structure. The formation of a metastable amorphous/semi-crystalline phase was observed prior to crystallization for glasses with avalanche mode of nucleation.<sup>9</sup> Recently, Jiang et al.<sup>10</sup> investigated the isothermal annealing process of  $Cu_{47.5}Zr_{45.1}Al_{7.4}$  BMG; they discovered that crystallization began with the formation of  $(Cu, Al)_{10}Zr_7$  and then progressed to the creation of  $CuZr_2$  and  $AlCu_2Zr$ . They also identified that a new liquid phase, characterized by enhanced local order and obscure compositional changes, emerged from the supercooled liquid before crystallization.

The formation of crystalline precipitates in BMGs unfolds through two processes. The first involves structural ordering during which the atomic packing becomes ordered with long-range order developing within the precipitates. The second process entails the redistribution of chemical elements, aligning the composition of the precipitates with that of the crystalline phase. These two processes do not necessarily occur simultaneously. For example, in Vit 1 and Vit 4 BMGs, phase separation preceded the formation of nucleation sites for the crystalline phase, as shown by interference maxima observed in the small-angle scattering profiles.<sup>11</sup> In contrast, our recent study on  $Zr_{45.5}Cu_{45.5}Al_9$  BMG during isothermal annealing in the supercooled liquid region, using simultaneous differential scanning calorimetry (DSC) and small-angle neutron scattering (SANS), identified continuous chemical redistribution following amorphous-to-crystalline structural ordering. Furthermore, a transition region was observed, differing in composition yet sharing the same crystal structure with the final thermodynamically stable crystalline phase, suggesting its role as a precursor to enhance resistance to crystallization.<sup>12</sup> This finding revitalizes our

comprehension of the crystallization mechanisms of the existing Zr-Cu-Al alloys, prompting a reevaluation of their crystallization process.

This insight underscores the importance of chemical redistribution after structural ordering in maintaining the amorphous state and possibly influencing GFA. Predicting GFA has been a challenging yet critical endeavor for metallic glasses; this has prompted efforts towards predicting GFA<sup>13-25</sup> with several criteria for GFA evaluation having been proposed.<sup>26-33</sup> However, none of these criteria can accurately predict every known glass former, nor have any of them gained widespread acceptance as a dependable tool for predicting new metallic glass compositions. Our study aims to enrich the understanding of glass formation and offer experimental insights that will contribute to the development of new criteria for GFA evaluation.

We have specifically explored the structural evolution of  $Zr_{56}Cu_{36}Al_8$  and  $Zr_{46}Cu_{46}Al_8$  BMGs upon isothermal annealing in the supercooled liquid region using in situ simultaneous DSC and SANS technique, along with x-ray diffraction (XRD). Our findings have revealed divergent crystallization pathways for the two glasses.  $Zr_{46}Cu_{46}Al_8$ , exhibiting better GFA, underwent a complex crystallization process characterized by the development of a transition region, which has a composition differing from but sharing the same crystal structure as the final thermodynamically stable phase, serving as a precursor that eventually transformed to the final stable crystalline phase of  $Cu_{10}Zr_7$  through continuous chemical redistribution during the late stage of annealing. In contrast,  $Zr_{56}Cu_{36}Al_8$ , a poor glass former, transformed directly from the amorphous phase to the final crystalline phase,  $CuZr_2$ , without any observable chemical redistribution.

## MATERIALS AND METHODS

Alloy ingots with nominal compositions of  $Zr_{46}Cu_{46}Al_8$  (at.%) and  $Zr_{56}Cu_{36}Al_8$  (at.%) were prepared by arc melting a mixture of Zr (99.99%), Cu (99.99%), and Al (99.99%) in a Ti-gettered argon atmosphere and then homogenized by re-melting and quenched into a copper mold by suction casting under a high-purity Ar atmosphere. The cast samples are cylindrical in form, measuring approximately 3 mm in diameter and 70 mm in length. The onset temperatures for the glass transition of  $Zr_{56}Cu_{36}Al_8$  and  $Zr_{46}Cu_{46}Al_8$ , as determined by DSC at a heating rate of 10 K/min, were 667 K and 697 K, respectively, according to Ref. 7. Prior to conducting in situ experiments, the as-cast samples were initially examined by x-ray diffraction (XRD, Bruker D2 PHASER) to verify their amorphous characteristics.

The QUOKKA instrument<sup>34,35</sup> at the OPAL reactor, Australian Nuclear Science and Technology Organisation (ANSTO), was employed for in situ simultaneous DSC and SANS experiments. The

neutron beam utilized had a diameter of 5 mm, with a wavelength of 5 Å and wavelength resolution of 10%. Both the source-to-sample and sample-to-detector distances were set to 10 m. For the experiments, thin plate samples measuring  $6 \times 3 \times 1 \text{ mm}^3$  were positioned in a quartz DSC cell within a custom-designed DSC furnace, equipped with a liquid nitrogen cooling system.<sup>36</sup> Regarding the isothermal annealing process, the samples were heated at a heating rate of 10 K/min to temperatures approximately 20 K above their respective glass transition temperatures, specially 692 K for  $\text{Zr}_{56}\text{Cu}_{36}\text{Al}_8$  and 718 K for  $\text{Zr}_{46}\text{Cu}_{46}\text{Al}_8$ , situated within the supercooled liquid regions. Upon reaching the target temperatures, the samples were held at these levels for a predetermined period to facilitate the annealing process. Afterwards, the samples were cooled back to room temperature at a rate of 20 K/min. DSC data were gathered with a high temporal resolution of 1 s throughout the annealing process. Concurrently, SANS data were compiled into a single streamed data file using event mode acquisition. To enhance statistical accuracy, the SANS data were post-experimentally binned in 1-min increments and utilized for subsequent data reduction and analysis. Data reduction and analysis were conducted using Igor Pro software,<sup>37</sup> incorporating a QUOKKA-specific reduction package built upon NCNR macros. To perform SANS data reduction, the initially obtained two-dimensional scattering patterns were first corrected for the blocked beam, detector efficiency, and background scattering, followed by azimuthal integration. The resulting one-dimensional profiles, denoted as  $I(Q)$ , spanned a  $Q$  range from  $0.00729 \text{ \AA}^{-1}$  to  $0.10000 \text{ \AA}^{-1}$  ( $Q = 4\pi\sin\theta/\lambda$ , with  $\theta$  being half of the scattering angle). The scattering intensity of the sample ( $I_s$ ) is calculated using the formula:

$$I_s = [I_{s+\text{cell}}(t) - I_{\text{blocked}}]/T_{s+\text{cell}}(t_0) - [I_{\text{cell}}(t) - I_{\text{blocked}}]/T_{\text{cell}}(t_0) \quad (1)$$

where  $I_s$ ,  $I_{\text{cell}}$ , and  $I_{s+\text{cell}}$  represent the scattering of sample, cell, and sample in a quartz cell, respectively.  $I_{\text{blocked}}$ , which denotes the blocked beam, refers to the intensity measured when the direct path of the beam is intentionally blocked by a neutron absorber before it reaches the sample to account for non-sample background effects such as cosmic radiation.  $T_{\text{cell}}$  and  $T_{s+\text{cell}}$  are the transmission values of the cell and sample within the quartz cell, respectively.  $t_0$  is the time at which the sample reaches the isothermal annealing temperature. In the following text,  $t_0$  is designated as 0 min.

After conducting simultaneous DSC and SANS measurements, the annealed samples were further examined by XRD. The XRD measurements were carried out employing a Rigaku SmartLab X-ray diffractometer, utilizing Cu  $K_\alpha$  radiation, under the operational conditions of 45 kV and 200 mA.

The diffraction patterns were collected over a  $2\theta$  range of  $20\text{--}80^\circ$  with a step width of  $0.01^\circ$  and a scan speed of  $2^\circ/\text{min}$ .

In the following, for convenience of discussion,  $\text{Zr}_{56}\text{Cu}_{36}\text{Al}_8$  and  $\text{Zr}_{46}\text{Cu}_{46}\text{Al}_8$  are abbreviated as Zr56 and Zr46, respectively.

## RESULTS

The amorphous structure of metallic glasses is commonly examined by XRD. Figure 1a shows the XRD patterns for the as-cast Zr56 and Zr46 alloys, highlighted by two notable broad peaks. This characteristic confirms the samples' amorphous nature, indicating the absence of a crystalline structure within the samples. Additionally, their amorphous nature was confirmed by SANS. As illustrated in Fig. 1b, although both alloys showed a slight increase in scattering intensity at low  $Q$  values, which was attributed to the scattering from sample imperfections,<sup>38</sup> the two alloys exhibited minimal scattering across the entire  $Q$  range, indicative of an amorphous structure. Figure 1c shows the DSC traces of the as-cast Zr56 and Zr46 alloys during isothermal annealing in the supercooled liquid region. Upon annealing, both samples exhibited clear exothermic peaks characteristic of crystallization.

Figure 2 presents the time-resolved integrated signals from simultaneous DSC and SANS measurements on Zr56 and Zr46 alloys during isothermal annealing. The integration of DSC data, indicated by solid lines, was achieved by calculating the area under the exothermic peaks in the DSC traces, which signifies the heat release associated with crystallization. Meanwhile, the integration of SANS data, represented by open circles, was derived by integrating the scattering intensity across the full accessible  $Q$  range of  $0.00729\text{--}0.10000 \text{ \AA}^{-1}$ , elucidating nanoscale density fluctuations. Based on the integration results of the DSC data, the starting and ending times of heat release for both alloys were determined and indicated by dashed lines and arrows. For Zr56, the starting and ending times are 40 min and 90 min, respectively. For Zr46, the heat release started at 47 min and ended at 94 min. Also, during the annealing process, the release of heat from crystallization and increase in small-angle scattering intensity due to nanoscale density fluctuations coincide, which is consistent with our previous study on  $\text{Zr}_{45.5}\text{Cu}_{45.5}\text{Al}_9$  BMG.<sup>12</sup> However, after heat release, Zr56 and Zr46 show different development of SANS intensity. The scattering intensity of Zr56 remained steady, whereas for Zr46, it exhibited a continual rise, albeit with a progressively diminishing rate of increase. This variance underscores the differing nanoscale structural evolutions in the two alloys following the heat release associated with crystallization.

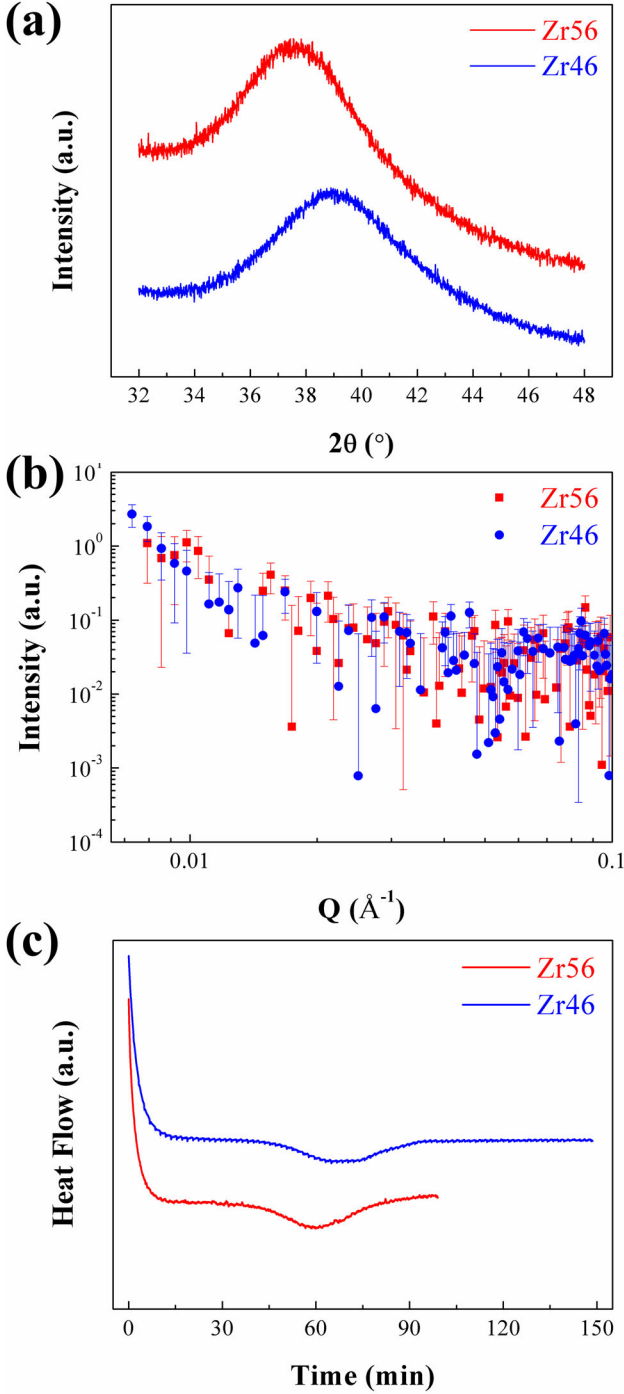


Fig. 1. (a) XRD patterns and (b) SANS profiles of as-cast Zr56 and Zr46 alloys. (c) DSC data of Zr56 (red) and Zr46 (blue) alloys during isothermal annealing in the supercooled liquid region (Color figure online).

To further elucidate the scattering intensity variation observed in the Zr46 alloy throughout the isothermal annealing process, we applied model fitting to its scattering profiles, aiming to unravel the structural evolution. This analysis presupposes the simplest possible morphology, namely that the

crystalline particles emerging within the alloy were spherical and adhered to a lognormal size distribution. The model incorporates a Porod law function to address scattering intensity from large structural inhomogeneities with sharp interfaces, employs a lognormal distribution for the size variation of spherical crystalline particles, and includes a flat background to account for the baseline scattering intensity:

$$I(Q) = A \times Q^{-4} + (B/\langle V \rangle) \times \int_0^\infty f(R)(\Delta\rho)^2 V^2 [F(Q, R)]^2 dR + C \quad (2)$$

where  $A$ ,  $B$  are scale factors,  $\Delta\rho$  denotes the scattering length density difference between the crystalline particles and the surrounding amorphous matrix,  $F(Q, R)$  represents the form factor amplitude for a sphere, i.e.,  $F(Q, R) = 3[\sin(QR) - QR\cos(QR)]/(QR)^3$ , and  $C$  accounts for the constant background scattering. The lognormal size distribution for the crystalline particles,  $f(R)$ , is defined as  $f(R) = [1/(\sigma R\sqrt{2\pi})] \times \exp[-(\ln R - \ln R_{\text{med}})^2/2\sigma^2]$ , where  $R_{\text{med}}$  and  $\sigma$  represent the median radius and polydispersity of the crystalline particles, respectively. The average particle volume,  $\langle V \rangle$ , is calculated using  $\langle V \rangle = 4\pi\langle R^3 \rangle/3$ , with  $\langle R^3 \rangle = (R_{\text{med}})^3 \times \exp(9\sigma^2/2)$ . The model yielded satisfactory fits to the scattering data, as demonstrated by two examples in Fig. 3a; note that, for improved visual representation, the scattering data collected at 150 min have been arbitrarily adjusted by multiplying by a constant. Figure 3b and d depicts the temporal evolution of the mean particle radius ( $R_{\text{avg}}$ ) and the corresponding polydispersity ( $\sigma$ ). Upon annealing, it was observed that the size of the crystalline particles initially increased before reaching a stable state. Furthermore, as the annealing time progressed, the size distribution of these particles remained unchanged, corresponding to the size distribution curves presented in Fig. 3c. Ultimately, the crystalline particles within the alloy stabilized at an average radius ( $R_{\text{avg}}$ ) of approximately 73 Å with a polydispersity ( $\sigma$ ) of about 0.63.

After completing the simultaneous DSC and SANS measurements, the annealed samples were further examined through XRD. Employing Rietveld refinement,<sup>39</sup> a powerful technique for phase analysis, Fig. 4 shows the refined XRD patterns of the annealed Zr56 and Zr46 alloys, revealing that the samples had not achieved full crystallization. As expected, the crystalline product of the Zr56 alloy closely matched the tetragonal  $\text{CuZr}_2$  phase, whereas the crystalline product of the Zr46 alloy was closely aligned with the orthorhombic  $\text{Cu}_{10}\text{Zr}_7$  phase, in agreement with the phases identified in earlier research.<sup>7</sup> The goodness of fit values, 2.12 for Zr56 and 2.34 for Zr46, indicate good agreement between the experimental results and the calculated diffraction patterns.

## DISCUSSION

### Different Crystallization Pathways

Figure 2 shows that the scattering intensity of Zr46 continues to increase even after exothermic release reaches a plateau. To comprehensively analyze the data obtained from simultaneous DSC and SANS measurements, we consolidated the key observations, as depicted in Fig. 5. It is evident that the average radius of the crystalline particles in the Zr46 alloy initially increased and then stabilized, reaching a steady state after approximately 94 min of annealing. This indicates a diffusion-controlled process with soft impingement occurring between the crystalline particles.<sup>8</sup> Taking the results together, a three-stage structural evolution of the Zr46 alloy during isothermal annealing is proposed. In Stage I, the incubation period from 0 min to 47 min, there is no heat release and only negligible changes in SANS intensity are observed. Stage II marks the process of amorphous-to-crystalline structural ordering, characterized by significant heat release and a marked increase in SANS intensity. Stage III is identified by a sustained increase in SANS intensity, with no additional heat release, indicating no further crystal nucleation and growth. Similar behavior has been observed in multicomponent  $\text{Zr}_{52.5}\text{Cu}_{17.9}\text{Ni}_{14.6}\text{Al}_{10}\text{Ti}_5$ <sup>40</sup> and  $\text{Zr}_{42.6}\text{Ti}_{12.4}\text{Cu}_{11.25}\text{Ni}_{10}\text{Be}_{23.75}$ <sup>11</sup> BMGs.

As detailed in Ref. 12, the scattering intensity,  $I(Q)$ , is influenced by the number density of the crystalline particles, composition and density differences between the particles and the matrix (scattering contrast  $(\Delta\rho)^2$ ), and particle volume. By Stage III, the stable particle size and absence of nucleation imply that the increase in  $I(Q)$  results from enhanced scattering contrast because of

continuous chemical redistribution within the alloy, making this the continuous chemical redistribution stage. Initially, during Stage II, an orthorhombic lattice structure with a thermodynamically unfavorable composition, termed the ‘transition region,’ is formed; through chemical redistribution in Stage III, this evolves into the final, stable crystalline phase of  $(\text{Cu, Al})_{10}\text{Zr}_7$ . This progression aligns with the crystallization pathway observed for the  $\text{Zr}_{45.5}\text{Cu}_{45.5}\text{Al}_9$  alloy.<sup>12</sup>

Differently, the Zr56 alloy demonstrated a different behavior during its isothermal annealing process, as evidenced by the unchanging SANS intensity beyond 90 min, which is depicted in Fig. 2. This constancy in SANS intensity suggests that, in contrast to Zr46, Zr56 does not undergo chemical redistribution during its annealing process. The annealing process of this alloy was characterized by just two stages: Stage I, the incubation stage, during which no noticeable changes were observed, and Stage II, in which the transition from an amorphous to a crystalline state took place, often referred to as crystallization. The transition to the crystalline state in the Zr56 alloy resulted in the formation of the tetragonal  $\text{CuZr}_2$  phase (Fig. 4). Remarkably, the evolution towards this tetragonal lattice structure with a thermodynamically stable composition appeared to occur directly without intermediate stages involving chemical redistribution. This direct path to the formation of a stable crystalline phase is supported by the DSC results presented in Fig. 1.

### Kinetics Consideration of the Occurrence of the Continuous Chemical Redistribution

According to the XRD results in Fig. 1, it is evident that compared to Zr56, the amorphous peak of Zr46 shifts to higher angles, with the angle corresponding to the highest value of the peak increasing from approximately  $37.5^\circ$  to around  $39^\circ$ . This shift suggests that the atomic volume of Zr46 is smaller than that of Zr56,<sup>41</sup> indicating a larger packing fraction for Zr46.<sup>42</sup> Therefore, the atomic diffusivity in Zr46 is believed to be slower.

Diffusion plays a critical role in the crystallization process of BMGs. To facilitate the formation of the corresponding stable crystalline phase, the Zr46 alloy must eject Zr and Al atoms into the surroundings through long-range diffusion, in contrast to the Zr56 alloy, which requires the expulsion of Cu atoms. Given that Zr and Al atoms are larger, Cu atoms are more mobile and diffuse more readily.<sup>43,44</sup> Consequently, the diffusion rate in the Zr46 alloy is lower than in the Zr56 alloy,<sup>7</sup> consistent with the XRD results (Fig. 1).

In the Zr46 alloy, the lower diffusion rate hinders rapid crystallization, allowing for the formation and subsequent transformation of transition regions. Since these transition regions have a composition different from that of the thermodynamically

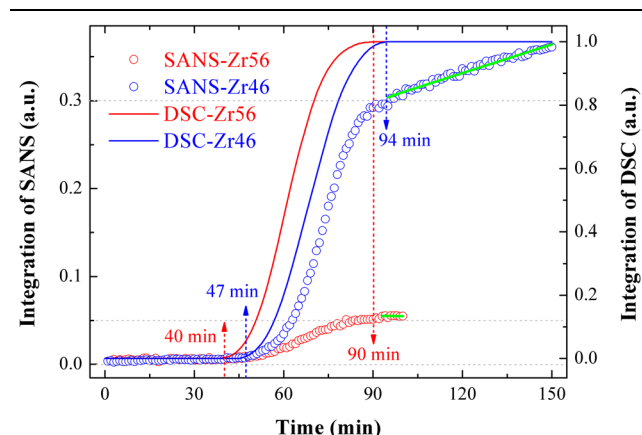


Fig. 2. Summarized results from DSC and SANS of Zr56 (red) and Zr46 (blue) alloys. The integration of DSC data is shown by solid lines, and the integration of SANS data is shown by open circles. The dashed lines and arrows indicate the starting and ending times of heat release for the two alloys upon isothermal annealing in the supercooled liquid region. The green lines are drawn to guide the eyes (Color figure online).

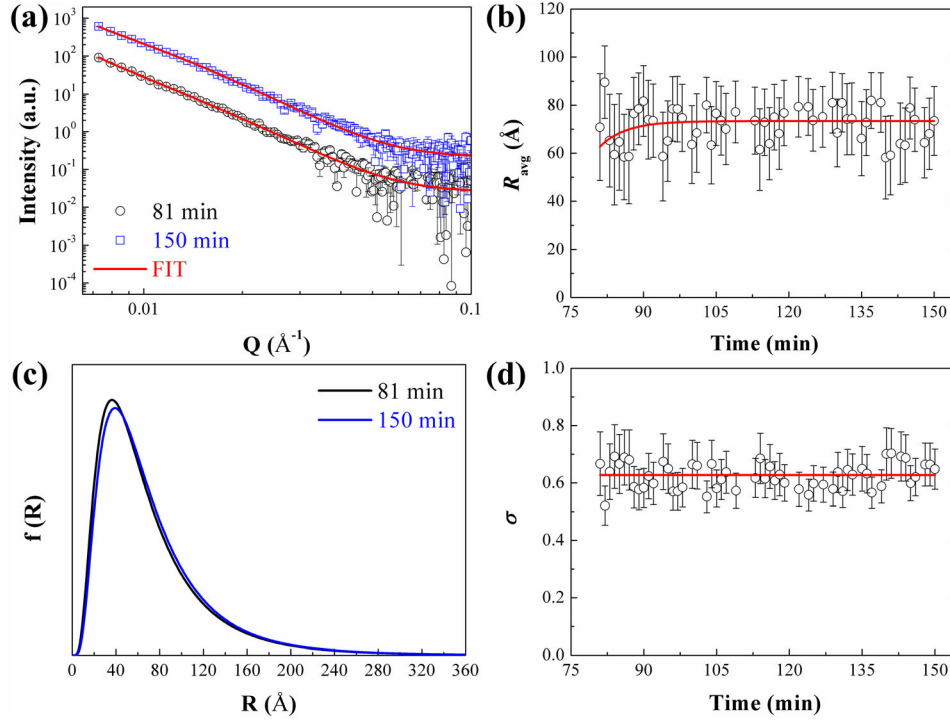


Fig. 3. SANS data analysis of Zr46 alloy. (a) Experimental SANS data (symbols) collected at 81 and 150 min of annealing, with model fits (red solid lines) that include a Porod law function, a lognormal distribution of spheres, and a flat background. Note that 150-min data have been shifted vertically for clarity. The associated particle size distributions  $f(R)$  are depicted in (c). (b) and (d) Mean radius  $R_{\text{avg}}$  and polydispersity  $\sigma$ , respectively, over time, derived from the model fitting. The red solid curves are drawn as a visual guide (Color figure online).

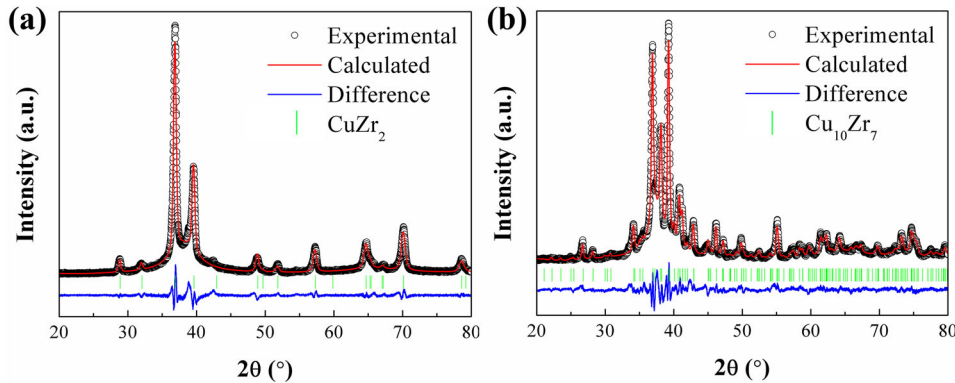


Fig. 4. Rietveld refinement of XRD patterns for the annealed Zr56 (a) and Zr46 (b) alloys. The experimental data points are represented by open circles, with the calculated patterns shown by red solid lines. The positions of Bragg peaks for the  $\text{CuZr}_2$  and  $\text{Cu}_{10}\text{Zr}_7$  phases are marked by green vertical bars. The difference plot illustrating the deviations between the experimental data and the calculated pattern is shown at the bottom (Color figure online).

stable crystalline phase, to reduce the system's Gibbs free energy, these transition regions evolve into the final stable crystalline phase through continuous chemical redistribution. In contrast, the Zr56 alloy, with its faster diffusion rate, undergoes a more direct and rapid crystallization process. The absence of continuous chemical redistribution and intermediate transition regions results in a straightforward transformation to the thermodynamically stable crystalline phase.

### Link Between Continuous Chemical Redistribution and Glass Forming Ability

Continuous chemical redistribution following structural ordering appears closely linked with the GFA of BMGs. Specifically, Zr46, identified as a good glass former, exhibited a three-stage structural evolution during isothermal annealing, with continuous chemical redistribution occurring at the late stage. This process involved the formation of a transition region, with the continuous chemical

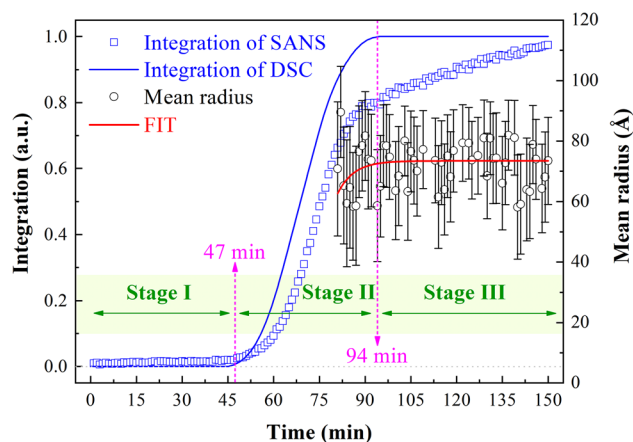


Fig. 5. Summarized data of DSC and SANS for  $Zr_{46}$  alloy. The integration of DSC data is shown by blue solid line, and the integration of SANS data is shown by open squares. The dashed lines and arrows mark the starting and ending times of heat release for the alloy upon isothermal annealing in the supercooled liquid region. The mean particle radius is shown by black open circles, and the red line is drawn as a guide to the eye (Color figure online).

redistribution process facilitating the transition to the equilibrium state, while,  $Zr_{56}$ , a poor glass former, underwent a straightforward transformation from the amorphous to the thermodynamically stable crystalline state, without any evidence of continuous chemical redistribution, exhibiting little resistance against crystallization. This suggests that the continuous chemical redistribution process plays a crucial role in stabilizing the amorphous state, thereby enhancing the thermal stability of BMGs. The occurrence of such chemical redistribution at the late stage of annealing not only underlines a mechanism that prevents premature crystallization but also potentially offers a viable criterion for evaluating the GFA of BMGs. Thus, continuous chemical redistribution emerges as a key factor in sustaining the amorphous structure, serving as an indicator of a BMG's ability to resist crystallization and maintain its glassy state.

### Implications for Future Studies

In this study, we have employed advanced in situ simultaneous DSC and SANS techniques to capture both thermal transitions and nanoscale structural evolution concurrently, enabling us to investigate the structural evolution stages of BMGs during isothermal annealing. Notably, we have hypothesized that continuous chemical redistribution at the late stage of annealing could serve as a practical criterion for evaluating the GFA of BMGs. The presence of such redistribution suggests high GFA, while its absence typically indicates a lower GFA and a greater likelihood of crystallization.

Understanding the atomic-level mechanisms underlying the continuous chemical redistribution

process in BMGs during isothermal annealing is therefore crucial. This insight encourages subsequent researchers to utilize advanced techniques such as aberration-corrected transmission electron microscopy and atom probe tomography to gain valuable insights into atomic rearrangement and diffusion pathways during annealing. Tailoring alloy compositions and annealing conditions to regulate continuous chemical redistribution can provide theoretical guidance for developing BMGs with exceptional performance suitable for various applications.

### CONCLUSION

In summary, the structural evolution of  $Zr_{56}Cu_{36}Al_8$  and  $Zr_{46}Cu_{46}Al_8$  BMGs upon isothermal annealing in the supercooled liquid region was investigated by in situ simultaneous DSC and SANS, complemented by XRD analysis. The main conclusions are summarized as follows:

- (1) The  $Zr_{46}Cu_{46}Al_8$ 's structural evolution during isothermal annealing was processed through three stages: (1) the incubation stage; (2) amorphous-to-crystalline structural ordering; (3) continuous chemical redistribution stage. In contrast, no feature of continuous chemical redistribution was observed in  $Zr_{56}Cu_{36}Al_8$ .
- (2)  $Zr_{46}Cu_{46}Al_8$ , identified as a good glass former, underwent a complex crystallization process characterized by the development of a transition region, which evolved into the final thermodynamically stable crystalline phase of  $Cu_{10}Zr_7$  through continuous chemical redistribution at the late stage of annealing. In contrast,  $Zr_{56}Cu_{36}Al_8$ , a poor glass former, transformed directly from the amorphous phase to a thermodynamically stable crystalline phase of  $CuZr_2$ , without late-stage chemical redistribution.
- (3) Continuous chemical redistribution at the late stage of annealing could serve as a practical criterion for evaluating the GFA of BMGs. The presence of such redistribution suggests high GFA, while its absence typically indicates a lower GFA and a greater likelihood of crystallization.

These findings underscore the importance of chemical redistribution in the crystallization process of BMGs, highlighting their potential role in evaluating their glass-forming abilities and facilitating the development of new BMGs with optimized properties.

### ACKNOWLEDGEMENTS

This work was supported by the Research Grants Council of Hong Kong Special Administrative Region, Project N\_CityU173/22. S. Lan acknowledges the supports by the National Natural Science Foundation of China (Grant Nos. 52222104, 12261160364). Z.D. Wu acknowledges the financial

support by the National Natural Science Foundation of China (Grant No. 52201190) and the open research fund of Songshan Lake Materials Laboratory (Grant No. 2022SLABFN19). C.C. Yuan acknowledges the financial support by the National Natural Science Foundation of China (Grant No. 52071078). X.L. Wu acknowledges the Start-up Fund from Anhui University of Technology (Grant No. DT2300000362). We acknowledge the support of the Australian Centre for Neutron Scattering, Australian Nuclear Science and Technology Organization, through proposal number 4707 in providing the neutron-scattering research facilities.

### CONFLICT OF INTEREST

The authors declare that they have no conflict of interest.

### REFERENCES

1. A. Inoue, *Acta Mater.* 48(1), 279 (2000).
2. D. Wang, H. Tan, and Y. Li, *Acta Mater.* 53(10), 2969 (2005).
3. P. Yu, H.Y. Bai, M.B. Tang, W.H. Wang, and J. Non-Cryst. Solids 351(14–15), 1328 (2005).
4. G. Kumar, T. Ohkubo, T. Mukai, and K. Hono, *Scripta Mater.* 57(2), 173 (2007).
5. H.B. Yu, W.H. Wang, and H.Y. Bai, *Appl. Phys. Lett.* 96(8), 081902 (2010).
6. Y. Wu, H. Wang, H.H. Wu, Z.Y. Zhang, X.D. Hui, G.L. Chen, D. Ma, X.L. Wang, and Z.P. Lu, *Acta Mater.* 59(8), 2928 (2011).
7. S. Lan, X.Y. Wei, J. Zhou, Z.P. Lu, X.L. Wu, M. Feyngenson, J. Neufeind, and X.L. Wang, *Appl. Phys. Lett.* 105(20), 201906 (2014).
8. X.L. Wu, S. Lan, X.Y. Wei, J. Zhou, Z.P. Lu, J.D. Almer, and X.L. Wang, *Appl. Phys. Lett.* 114(21), 211903 (2019).
9. S. Lan, Z.D. Wu, X.Y. Wei, J. Zhou, Z.P. Lu, J. Neufeind, and X.L. Wang, *Acta Mater.* 149, 108 (2018).
10. H.R. Jiang, J. Tseng, N. Neuber, J. Barrirero, B. Adam, M. Frey, A.C. Dippel, S. Banerjee, I. Gallino, A.H. Feng, G. Wang, F. Mücklich, R. Busch, and J. Shen, *Acta Mater.* 226, 117668 (2022).
11. J.F. Löffler, and W.L. Johnson, *Mater. Sci. Eng. A* 304–306, 670 (2001).
12. X.L. Wu, S. Lan, X.Y. Li, M. Yang, Z.D. Wu, X.Y. Wei, H.Y. He, M. Naeem, J. Zhou, Z.P. Lu, E.P. Gilbert, D. Ma, and X.-L. Wang, *J. Mater. Sci. Technol.* 101, 285 (2022).
13. L. Xia, S.S. Fang, Q. Wang, Y.D. Dong, and C.T. Liu, *Appl. Phys. Lett.* 88, 171905 (2006).
14. E.S. Park, J.H. Na, and D.H. Kim, *Appl. Phys. Lett.* 91, 031907 (2007).
15. Y. Li, Q. Guo, J.A. Kalb, and C.V. Thompson, *Science* 322, 1816 (2008).
16. D. Ma, A.D. Stoica, X.L. Wang, Z.P. Lu, M. Xu, and M. Kramer, *Phys. Rev. B* 80(1), 014202 (2009).
17. J. Cheneya, and K. Vecchio, *J. Alloy. Compd.* 471, 222 (2009).
18. D.B. Miracle, D.V. Louzguine-Luzgin, L.V. Louzguina-Luzgina, and A. Inoue, *Int. Mater. Rev.* 55(4), 218 (2010).
19. K.J. Laws, D.B. Miracle, and M. Ferry, *Nat. Commun.* 6, 8123 (2015).
20. E. Perim, D.W. Lee, Y.H. Liu, C. Toher, P. Gong, Y.L. Li, W.N. Simmons, O. Levy, J.J. Vlassak, J. Schroers, and S. Curtarolo, *Nat. Commun.* 7, 12315 (2016).
21. W.L. Johnson, J.H. Na, and M.D. Demetriou, *Nat. Commun.* 7, 10313 (2016).
22. R.J. Deng, Z.L. Long, L. Peng, D.M. Kuang, B.Y. Ren, and J. Non-Cryst. Solids 533, 119829 (2020).
23. J. Xiong, S.Q. Shi, and T.Y. Zhang, *Comp. Mater. Sci.* 192, 110362 (2021).
24. Y.X. Zhang, G.C. Xing, Z.D. Sha, and L.H. Poh, *J. Alloy. Compd.* 875, 160040 (2021).
25. M.X. Li, Y.T. Sun, C. Wang, L.W. Hu, S. Sohn, W.H. Jan Schroers, and Y.H.L. Wang, *Nat. Mater.* 21, 165 (2022).
26. D. Turnbull, and M.H. Cohen, *J. Chem. Phys.* 34(1), 120 (1961).
27. Z.P. Lu, and C.T. Liu, *Acta Mater.* 50(13), 3501 (2002).
28. Q.J. Chen, J. Shen, D.L. Zhang, H.B. Fan, J.F. Sun, and D.G. McCartney, *Mat. Sci. Eng. A* 433(1–2), 155 (2006).
29. X.H. Du, J.C. Huang, C.T. Liu, and Z.P. Lu, *J. Appl. Phys.* 101(8), 086108 (2007).
30. Z.Z. Yuan, S.L. Bao, Y. Lu, D.P. Zhang, and L. Yao, *J. Alloy. Compd.* 459(1–2), 251 (2008).
31. Z.L. Long, H.Q. Wei, Y.H. Ding, P. Zhang, G.Q. Xie, and A. Inoue, *J. Alloy. Compd.* 475(1–2), 207 (2009).
32. S. Guo, and C.T. Liu, *Intermetallics* 18(11), 2065 (2010).
33. B.Y. Ren, Z.L. Long, and R.J. Deng, *Comput. Mater. Sci.* 189, 110259 (2021).
34. S.A. Pullen, N. Booth, S.R. Olsen, B. Day, F. Franceschini, D. Mannicke, and E.P. Gilbert, *Meas. Sci. Technol.* 25(5), 055606 (2014).
35. K. Wood, J.P. Mata, C.J. Garvey, C.M. Wu, W.A. Hamilton, P. Abbeywick, D. Bartlett, F. Bartsch, P. Baxter, N. Booth, W. Brown, J. Christoforidis, D. Clowes, T. d'Adam, F. Darmann, M. Deura, S. Harrison, N. Hauser, G. Horton, D. Federici, F. Franceschini, P. Hanson, E. Imamovic, P. Imperia, M. Jones, S. Kennedy, S. Kim, T. Lam, W.T. Lee, M. Lesha, D. Mannicke, T. Noakes, S.R. Olsen, J.C. Osborn, D. Penny, M. Perry, S.A. Pullen, R.A. Robinson, J.C. Schulz, N. Xiong, and E.P. Gilbert, *J. Appl. Crystallogr.* 51, 294 (2018).
36. ACNS User Portal: Sample Environment. <https://neutron.nstsl.gov.au/Bragg/proposal/Ancillaries.jsp?id=4&type=1>.
37. S.R. Kline, *J. Appl. Crystallogr.* 39, 895 (2006).
38. X.L. Wu, S. Lan, Z.D. Wu, X.Y. Wei, Y. Ren, H.Y. Tsang, and X.L. Wang, *Prog. Nat. Sci.-Mater.* 27(4), 482 (2017).
39. L.B. McCusker, R.B. Von Dreele, D.E. Cox, D. Louer, and P. Scardi, *J. Appl. Crystallogr.* 32, 36 (1999).
40. X.L. Wang, J. Almer, C.T. Liu, Y.D. Wang, J.K. Zhao, A.D. Stoica, D.R. Haefner, and W.H. Wang, *Phys. Rev. Lett.* 91, 265501 (2003).
41. D. Ma, A.D. Stoica, and X.L. Wang, *Nat. Mater.* 8, 30 (2009).
42. D. Ma, A.D. Stoica, and X.L. Wang, *Appl. Phys. Lett.* 91, 021905 (2007).
43. P. Thurnheer, R. Maaß, K.J. Laws, S. Pogatscher, and J.F. Löffler, *Acta Mater.* 96, 428 (2015).
44. S.V. Ketov, Y.P. Ivanov, B. Putz, Z. Zhang, J. Eckert, and A.L. Greer, *Acta Mater.* 214, 116993 (2021).

**Publisher's Note** Springer Nature remains neutral with regard to jurisdictional claims in published maps and institutional affiliations.

Springer Nature or its licensor (e.g. a society or other partner) holds exclusive rights to this article under a publishing agreement with the author(s) or other rightsholder(s); author self-archiving of the accepted manuscript version of this article is solely governed by the terms of such publishing agreement and applicable law.